

Background sky obscuration by cluster galaxies as a source of systematic error for weak lensing

Melanie Simet^{1*}, Rachel Mandelbaum¹

¹*McWilliams Center for Cosmology, Wean Hall, Carnegie Mellon University, 5000 Forbes Ave, Pittsburgh PA, USA, 15213*

20 June 2014

ABSTRACT

Lensing magnification and stacked shear measurements of galaxy clusters rely on measuring the density of background galaxies behind the clusters. The most common ways of measuring this quantity ignore the fact that some fraction of the sky is obscured by the cluster galaxies themselves, reducing the area in which background galaxies can be observed. We discuss the size of this effect in the Sloan Digital Sky Survey (SDSS) and the Canada-France-Hawaii Telescope Lensing Survey (CFHTLenS), finding a minimum 1 per cent effect at $0.1h^{-1}\text{Mpc}$ from the centers of clusters in SDSS; the effect is an order of magnitude higher in CFHTLenS. The resulting biases on cluster mass and concentration measurements are of the same order as the size of the obscuration effect, which is below the statistical errors for cluster lensing in SDSS but likely exceeds them for CFHTLenS. We also forecast the impact of this systematic error on cluster mass and magnification measurements in several upcoming surveys, and find that it typically exceeds the statistical errors. We conclude that future surveys must account for this effect in stacked lensing and magnification measurements in order to avoid being dominated by systematic error.

Key words: gravitational lensing: weak – methods: data analysis – galaxies: clusters: general

1 INTRODUCTION

Studies of galaxy clusters are powerful probes of cosmology (Albrecht et al. 2006; Allen et al. 2011) and dark matter physics (Voit 2005; Kravtsov & Borgani 2012), especially in combination with weak gravitational lensing measurements (Weinberg et al. 2013). However, accurate calibration of the cluster masses is critical, and requires a careful account of all sources of systematic error. Many studies have explored the impact of well-known sources of systematic uncertainty such as line-of-sight structure (Marian et al. 2010; Hoekstra et al. 2011), photometric redshift errors (Bernstein & Huterer 2010; Sheldon et al. 2012), triaxiality (Corless & King 2007; Hamana et al. 2012; Schneider et al. 2012), and cluster centroiding (Mandelbaum et al. 2010; George et al. 2012), as well as systematics general to weak lensing such as shape measurement bias (Bernstein & Jarvis 2002; Bridle et al. 2010; Kitching et al. 2012), detector effects (Massey et al. 2013), and intrinsic alignments (Hirata & Seljak 2004; Blazek et al. 2012; Heymans et al. 2013). We discuss here the impact of one particular systematic, the obscuration of part of the background sky by galaxies within the clus-

ters themselves due to the (in)ability of software to separate nearby galaxies (deblending).¹

As discussed further in section 2, magnification measurements (directly) and mass inference via stacked shear measurements (indirectly) depend on the observed number density of sources behind the galaxy clusters (Bartelmann & Schneider 2001; Schmidt et al. 2009; Sheldon et al. 2004). If the observed area is decreased due to an unaccounted-for obscuration by cluster galaxies, the number density errors can propagate back to the cosmological measurements of interest. Perniciously, the number density of galaxies in a cluster is a radius-dependent quantity which may mix into the radius-dependent magnification and lensing signals. The possibility of this obscuration effect has been noted before in Bartelmann & Schneider (2001, §1.2), Rozo et al. (2011, §3.5), and Applegate et al. (2014, §4.2), and has now been detected in the Dark Energy Survey (The Dark Energy Survey Collaboration 2005) in Melchior et al. (2014). The corrections required for this effect in the Melchior et al. cluster sample are as large as a

¹ Background galaxies may also be partially obscured by cluster dust, altering their colors and fluxes without impacting their detection levels, but we do not address this source of error in this work.

* msimet@andrew.cmu.edu

multiplicative factor of 3 in the inner regions of one cluster, and are non-negligible at $\leq 1h^{-1}\text{Mpc}$ for all clusters studied. We discuss this important measurement more in section 5.

We present a measurement of this effect in the Sloan Digital Sky Survey (SDSS; York et al. 2000) and explore how it should differ for the Canada-France-Hawaii Telescope Lensing Survey (CFHTLenS; Heymans et al. 2012). The CFHTLenS results are used to forecast the size of this effect in upcoming deep surveys. We discuss the theoretical underpinnings in section 2, describe the data sets in section 3, show results in section 4, and discuss implications for ongoing and future surveys such as the Hyper Suprime-Cam Survey (Miyazaki et al. 2012), the Dark Energy Survey, Euclid (Laureijs et al. 2011), and the Large Synoptic Survey Telescope (LSST; LSST Science Collaboration et al. 2009) in section 5.

2 THEORY

Weak lensing is the distortion of background galaxy shapes due to matter in foreground lenses such as galaxies and clusters. It is sensitive to the density profile of the lenses on small scales. A concentration of mass will distort the background galaxies to appear more tangentially aligned to the foreground lens than random galaxies would be, and so galaxy-galaxy or cluster-galaxy lensing attempts to measure this preferential alignment. In large surveys, where the signal to noise per foreground lens is small, lensing around galaxies or clusters involves stacking: the shears from all pairs of lenses and background galaxies in a given radius bin for a given lens sample are averaged to increase the signal-to-noise ratio. With stacking, ongoing and future surveys are expected to measure shear profiles with percent-level errors or better. Stacking also reduces the effect of some of the systematic errors, such as the large-scale structure contribution (which will have a different, uncorrelated sign and amplitude for the different lenses on small scales) and centroiding (provided that the centroiding errors can be characterized statistically for a large number of lenses).

For most cosmological analyses, we are in the thin lens limit, where the lenses are far from the observer and also far from the objects being lensed. In this case, we can describe the image distortions by a lensing potential,

$$\psi(\boldsymbol{\theta}) = \frac{1}{\pi} \int_{\mathbb{R}^2} d^2\theta' \frac{\Sigma(\boldsymbol{\theta}')}{\Sigma_{\text{cr}}} \ln |\boldsymbol{\theta} - \boldsymbol{\theta}'| \quad (1)$$

which depends on the surface mass density $\Sigma(\boldsymbol{\theta}')$ and a term called the critical density,

$$\Sigma_{\text{cr}} = \frac{c^2}{4\pi G} \frac{D_s}{D_l D_{ls}}, \quad (2)$$

which encodes the strength of the lensing signal as a function of the (angular diameter) distances in the problem. The ratio $\Sigma(\boldsymbol{\theta}')/\Sigma_{\text{cr}}$ is denoted κ and called the convergence. For axially symmetric lenses, the tangential shear (i.e., the measured coherent shape distortion of background galaxies) is

$$\gamma_t(R) = \bar{\kappa}(< R) - \kappa(R) \quad (3)$$

and for non-axially symmetric lenses the same relation holds as long as shears and convergences are azimuthally averaged.

We work here in the weak lensing limit, where these induced shears are of order 10 per cent or less of the RMS shear due to the intrinsic galaxy shapes.

In addition to the shape distortions, the observed galaxies are made larger by a factor $1 + \kappa$, which also increases the total observed flux (since lensing conserves surface brightness; Bartelmann & Schneider 2001). The measured number density of background galaxies under magnification, relative to the number density of background galaxies in the field, is increased due to the greater detectability of brighter and larger objects but decreased due to the overall number density reduction caused by the dilation of the background sky. If we assume the selection function for the galaxies included in the survey is a step function (size $r > r_{\text{min}}$, apparent magnitude $m < m_{\text{min}}$ or flux $f < f_{\text{min}}$), we can write the observed number density as (Schmidt et al. 2009)

$$n_{\text{obs}}(R) = n_0[1 + (2\beta_f + \beta_r - 2)\kappa(R)] \quad (4)$$

with

$$\begin{aligned} \beta_r &= -\left. \frac{\partial \ln n_{\text{obs}}}{\partial \ln r} \right|_{\substack{m < m_{\text{min}} \\ r = r_{\text{min}}}} \\ \beta_f &= -\left. \frac{\partial \ln n_{\text{obs}}}{\partial \ln f} \right|_{\substack{r > r_{\text{min}} \\ f = f_{\text{min}}}} = 2.5 \left. \frac{\partial \ln n_{\text{obs}}}{\partial m} \right|_{\substack{r > r_{\text{min}} \\ m = m_{\text{min}}}}. \end{aligned} \quad (5)$$

In practice, the number density is weighted to account for measurement errors in magnitude and photo- z . The partial derivatives above should be taken relative to the weighted (not raw) number density, which can make a significant difference in the measured parameter values.

Since a magnification measurement using number counts compares the observed surface number density of objects with some expected value for the field, the fraction of the sky that is obscured by cluster galaxies is a direct source of error. What one actually measures (when neglecting obscuration) is

$$\hat{n}_{\text{obs}}(R) = (1 - f_{\text{obs}})n_0(R)[1 + (2\beta_f + \beta_r - 2)\kappa(R)] \quad (6)$$

$$= (1 - f_{\text{obs}})n_{\text{obs}}(R). \quad (7)$$

Ideally, the convergence can be estimated via

$$\kappa = \frac{n_{\text{obs}} - n_0}{n_0 q} \equiv \frac{\delta n}{q} \quad (8)$$

where we define $q \equiv 2\beta_f + \beta_r - 2$ and galaxy number overdensity $\delta n \equiv n_{\text{obs}}/n_0 - 1$. When we use the incorrect estimator for \hat{n}_{obs} that does not account for the obscuration effect, Eq. 7, the estimated convergence becomes

$$\hat{\kappa}(R) = \frac{\hat{n}_{\text{obs}}(R)/n_0(R) - 1}{q} \quad (9)$$

$$= \frac{(1 - f_{\text{obs}})n_{\text{obs}}(R)/n_0(R) - 1}{q} \quad (10)$$

$$= (1 - f_{\text{obs}})\kappa(R) - \frac{f_{\text{obs}}}{q} \quad (11)$$

which is smaller than the true value.

For modeling $\kappa(R)$ we use a spherically symmetric Navarro-Frenk-White (NFW) density profile, which fits well with both simulations and previous measurements and which has an analytic solution (Wright & Brainerd 2000). We use a mass (defined using a spherical overdensity of $200\rho_{\text{crit}}$) of $10^{14}h^{-1}M_{\odot}$ and a concentration $c_{200} = 4$.

In principle, the estimated lensing shears $\gamma_{1,2}$ are independent of the obscuration of the background galaxies; they are, after all, typically estimated using averages of the observed galaxy shears. In practice, however, a correction must be made due to the use of photometric redshifts (photo-zs), and this correction relies on the number density of objects (Sheldon et al. 2004). The strength of the lensing signal depends on the redshifts through Σ_{cr}^{-1} , which is 0 for $z_{\text{source}} \leq z_{\text{lens}}$ and positive for $z_{\text{source}} > z_{\text{lens}}$. Photo-zs scatter physically associated (and therefore unlensed) galaxies in redshift space, so some unlensed galaxies with no expected signal will be included in the averaging intended to find the lensing signal, reducing the amplitude of the measurement. Near galaxy clusters—which contain many galaxies at the same redshift as the lens—the effect can be large, up to multiplicative factors of order a few (Parker et al. 2007; Sheldon et al. 2009). The exact magnitude of the effect depends on the photo-z quality and the typical line-of-sight separation between the sources and the lenses: higher photo-z errors or biases, and a large overlap between lens- and source-redshift distributions, will both increase the effect. A correction is usually made based on the weighted number density of objects around lenses compared to that around similarly distributed random points (Sheldon et al. 2004):

$$C(R) = \frac{N_{\text{rand}}}{N_{\text{lens}}} \frac{\sum_{\text{lens}} w_{\text{lens}}}{\sum_{\text{rand}} w_{\text{rand}}} \quad (12)$$

for lens-background galaxy pairs and random point-background galaxy pairs at radius R , which ties the measured shear to the measured number density. (Optimal weighting for this calculation involves not only the uncertainty on the shear, but also a weighting by the critical density through Σ_{cr}^{-2} .) Some authors (e.g. Rozo et al. 2011) include this correction directly in their cluster lensing shear estimator, rather than writing it as a separate correction factor, but both formalisms are attempting to account for the dilution of the lensing signal by physically associated sources, and are therefore subject to obscuration effects.

Given a factor f_{obs} , the fraction of the background sky obscured by galaxies within the galaxy cluster, the estimated $\hat{C}(R)$ while ignoring obscuration is actually

$$\hat{C}(R) = (1 - f_{\text{obs}})C(R). \quad (13)$$

However, ignoring the effect of magnification on the number counts will also lead to an error in the measured \hat{C} :

$$\hat{C}(R) = (1 - f_{\text{obs}})[1 + q\kappa(R)]C(R). \quad (14)$$

A slight subtlety is that the weights used to calculate the shear signals often differ from those used in estimates of magnification, so the relevant q in this equation may differ from what should be used in Eq. 10. Since some studies have already accounted for the effects of magnification on the number counts (e.g., Mandelbaum et al. 2006), we will directly compare the systematic error in the boost factor and therefore shear signal using Eq. 13 (obscuration effects alone) vs. Eq. 14 (obscuration effects and magnification), using the appropriately-weighted q for shear estimation.

3 DATA

We measure the obscuration effect with two surveys: the Sloan Digital Sky Survey (SDSS; York et al. 2000)

and the Canada-France-Hawaii Telescope Lensing Survey (CFHTLenS; Heymans et al. 2012). SDSS is wide but comparatively shallower, which will give us an idea of the problem in current stacked weak lensing measurements; CFHTLenS has a small area but is deeper, which will allow us to project the magnitude of the effect for upcoming surveys (section 5). Since magnification measurements are usually made on photometric samples, and shear measurements are usually made on shape samples that include additional selection criteria and/or weight factors, we will show results from both types of catalogue.

3.1 SDSS source catalogues

The shape catalogue from SDSS is described in Reyes et al. (2012). It contains 39 million galaxies in an area of 9243 deg² which pass photometry, shape noise and photo-z cuts, for an average density of 1.2 galaxies/arcmin². The limiting magnitude is $r < 21.8$. Typical seeing is 1.2 ± 0.2 arcsec. The data is processed through the **Photo v5.6** pipeline (Lupton et al. 2001; Stoughton et al. 2002; Aihara et al. 2011). Star-galaxy separation is performed using the **OBJC_TYPE** flag, which compares extended galaxy model fit magnitudes with PSF magnitudes. Shapes are then measured with the re-Gaussianization PSF correction software (Hirata & Seljak 2003). We do not use the shape measurements directly here, but we do use the errors on the shape measurement to define galaxy weights for the boost factor calculation (Eqn. 14). The weights also include the per-component intrinsic dispersion of galaxy shapes:

$$w_i = \frac{1}{e_{\text{rms}}^2 + \sigma_{e,i}^2}. \quad (15)$$

where, for this catalogue, we take $e_{\text{rms}} = 0.365$, consistent with the findings of Reyes et al. (2012). In addition, the traces of the moment matrices from the adaptive moments for the PSF (P) and image (I) are used to define a resolution factor,

$$R_2 = 1 - \frac{T_P}{T_I} \quad (16)$$

We use this as the size parameter for our magnification calculation with the SDSS shape (not photometric) catalogue, rather than, e.g., a measured galaxy radius, because this is the quantity that was used for galaxy selection. As discussed later in Section 4, we will also use it to determine an average PSF-convolved galaxy size. In practice, the cutoff for good shape measurement (and thus inclusion in our shape catalogue) is that $R_2 > 1/3$ in both r - and i -band imaging, so functionally we use (Mandelbaum et al. 2005)

$$R_{2,ri} = \min(R_{2,i}, R_{2,r}) \quad (17)$$

as the size parameter for our analysis. The weighted distributions $dN/d\text{mag}$ and $dN/d\log R_{2,ri}$, necessary for magnification, are shown in Fig. 1, and the derived parameters are given in Table 1. More details on the adaptive moments and the resolution calculation can be found in Mandelbaum et al. (2005) and Reyes et al. (2012).

For the corresponding photometric catalogue, we use a superset of the shape catalogue. We include the galaxies that did not pass the resolution cut (and have no measured shapes) in addition to the galaxies of the shape catalogue.

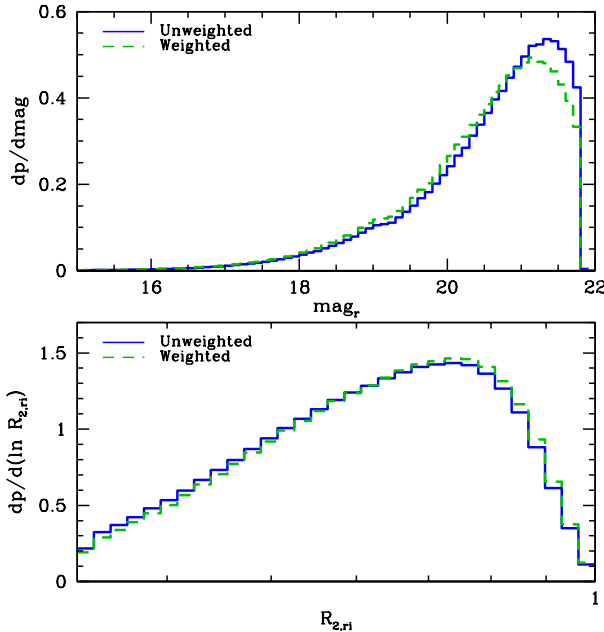


Figure 1. Weighted and unweighted distributions $dp/dmag$ and $dp/d \log R_{2,r}$ measurements for the SDSS shape catalogue, necessary for magnification calculations (Eq. 10).

	Shape		Photometric
	β_f	β_r	β_f
SDSS unweighted	1.1	0.22	1.9
SDSS weighted	0.89	0.19	3.1
CFHTLenS unweighted	1.3	0.14	1.8
CFHTLenS weighted	0.71	0.049	2.1

Table 1. Parameters for the magnification calculation, Eq. 10, as defined in Eq. 5 and calculated using the measurements in Fig. 2. These correspond to the slopes of $\log(\text{galaxy counts})$ relative to the magnitude (β_f) and galaxy size (β_r), up to multiplicative factors described in Eq. 5. Magnitude parameters were evaluated for the bin centred at $mag_r = 21.725$ (SDSS) and $mag_i = 24.575$ (CFHTLenS), as sharp drops in $dN/dmag$ were observed beyond those points, although a formal hard cutoff at the upper edges of those bins was not imposed in the rest of the analysis. The size parameters were both evaluated in the smallest bin included in the catalogue. Since there is no size cutoff in the photometric samples, we do not consider size magnification in that case.

For weights, we use the r -band photometric error plus a small intrinsic dispersion:

$$w_i = \frac{1}{0.02^2 + \sigma_{mag,i}^2}. \quad (18)$$

The photometric redshifts for this catalogue were generated with the Zurich Extragalactic Bayesian Redshift Analyzer (ZEBRA; Feldmann et al. 2006). Using the parameters described in Nakajima et al. (2012), ZEBRA makes a point estimate of the photo- z by fitting a set of templates to the observed galaxy colors (defined using corrected magnitudes from the PHOTO pipeline); the templates used here are from (Benítez 2000) and consist of four observed galaxy SEDs, two synthetic blue spectra, and 5 interpolated spec-

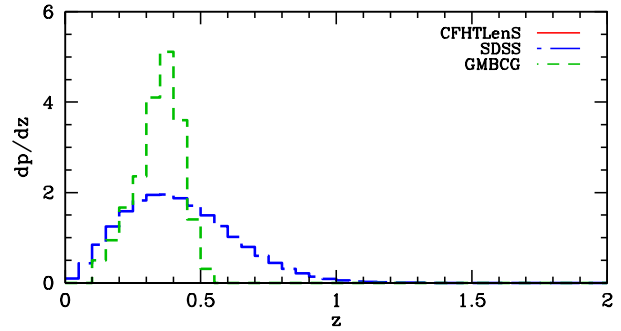


Figure 2. Unweighted redshift distributions (dp/dz) for the SDSS and CFHTLenS shape catalogues and GMBCG cluster catalogue. Photometric catalogues have a similar redshift distribution, with a slightly more populated high-redshift tail and a slightly less populated peak, but all such changes are at higher redshifts than the cluster sample.

tra in between each pair of the 6 spectra, for a total of 31 templates. The redshifts were validated against a set of spectroscopic and high-quality photometric redshifts with the same selection function as the source sample, which resulted in rejecting starburst-type galaxies (10 per cent of the sample) due to unreliability. The remaining galaxies have a small bias at $z \gtrsim 0.4$ which can be corrected for during lensing calculations through knowledge of the true dN/dz . The main effect in this analysis is the introduction of scatter in the optimal galaxy weighting (which depends on Σ_{cr}), which will reduce our signal-to-noise ratio. Further details of the photo- z catalogue can be found in Nakajima et al. (2012). The best-fit parameterized dN/dz from that paper for the SDSS shape catalogue can be found in Fig. 2; the functional form for the SDSS shape catalogue is a good fit for both the shape and photometric samples, although with slightly different parameter values.

3.2 SDSS cluster catalogue

Our cluster catalogue is the GMBCG catalogue (Hao et al. 2010). This catalogue contains approximately 51,000 galaxy clusters within the area of our SDSS shape catalogue. Clusters are chosen by fitting the color distribution of galaxies in a given patch of sky with a mixture of Gaussians; the field has a single broad Gaussian in color space, while clusters have an additional narrower Gaussian corresponding to the cluster red sequence. The red-sequence galaxies are then convolved by a projected NFW kernel to define a density, used as an estimator for the clustering strength at that location. Candidate brightest cluster galaxies (BCGs, found at the centers of many clusters; see, e.g., Kravtsov & Borgani 2012) are ranked by clustering strength, and then “percolated” down by removing candidate BCGs that appear in the clusters of more highly ranked BCG candidates. The cluster richness is then estimated in a two-step process of measuring cluster galaxies in a fixed aperture, then using that number to define a more appropriate radius and measuring the number of galaxies within the new aperture. The redshift distribution of these clusters is shown in Fig. 2. We

generate random points with the same area coverage as this catalogue using the SDSSPix software².

3.3 CFHTLenS source catalogues

We use the public data catalogue from the CFHTLenS project³ (Heymans et al. 2012). The catalogue consists of 22.7 million objects in the four fields of the CFHT Legacy Survey (CFHTLS), covering a total of 154 square degrees with a limiting magnitude of 24.7 and average seeing of $(0.6 - 0.65) \pm 0.1$ arcsec depending on field, both in the stacked i' -band. The stacked images contain fainter objects, but the 24.7 mag cut is imposed due to noise bias considerations for shape measurement and a lack of fainter photo- z training objects. The data-analysis pipeline, THELI, is described in Erben et al. (2013). In brief, objects are detected by running SExtractor (Bertin & Arnouts 1996) on a full-depth i' -band stack, and then shears are measured using the *lensfit* pipeline (Miller et al. 2013), which fits the object shapes simultaneously and jointly in the individual exposures using a Bayesian forward-modelling algorithm. The models used are two-component (bulge and disk) galaxy models, with the size and ellipticity as free parameters, marginalized over centroid position. The pipeline also generates a weight that includes the intrinsic shape dispersion as well as the *lensfit* measurement error, which we can use directly rather than making a calculation such as Eq. 15 for the measurements on the shape catalogue. For star-galaxy separation, we use the SExtractor CLASS_STAR for the photometric catalogue (where *lensfit* may not have run successfully) and the *lensfit* fitclass for the shape catalogue. Finally, for each object, a scalelength along the major axis is produced, with a hard lower cutoff at $r = 0.5$ pixels. This is the quantity we will use for the size magnification parameter in the shape catalogue. After cutting to objects classified as galaxies, we obtain a photometric catalogue of 15 million galaxies; after further removing galaxies with a *lensfit* weight of 0 and using the *lensfit* star-galaxy separation, 7.5 million galaxies remain (an unweighted number density of 13.5 galaxies/arcmin²) in our shape catalogue. The measurements of $dN/dmag$ and $dN/d \log r_{FWHM}$, necessary for magnification, are shown in Fig. 3, and the derived parameters are given in Table 1. The redshift distribution is shown in Fig. 2.

CFHTLenS photo- z s are measured using the Bayesian Photometric Redshift Code (BPZ; Benítez 2000; Coe et al. 2006) with colors measured using SExtractor in dual image mode on homogeneous Gaussianized versions of the stacked images in all bands (Hildebrandt et al. 2012). BPZ estimates a posterior likelihood by comparison with a set of templates; here the templates used are from Capak (2004). Comparison with spectroscopic and high-quality photometric redshifts shows strong agreement between the summed BPZ $P(z)$ s and the true redshift distribution, even for fairly narrow bands in peak BPZ redshift, for $0.2 < z_{BPZ} < 1.3$; redshifts beyond that range are significantly more uncertain. We use this redshift range in the rest of the analysis, as it is low redshift enough to detect galaxies in our cluster lensing sample,

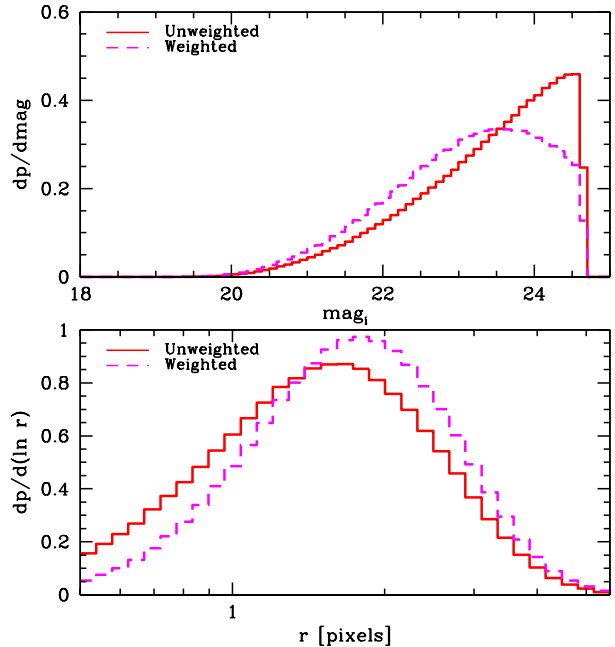


Figure 3. Weighted and unweighted distributions $dp/dmag$ and $dp/d \log r$ measurements for the CFHTLenS catalogue, necessary for magnification calculations (Eq. 10).

but also deep enough to investigate the magnification signal behind the clusters.

3.4 Cluster galaxy counts

Due to the conservative deblending settings used in the CFHTLenS pipeline, we cannot measure the obscuration effect well at $\lesssim 0.5h^{-1}$ Mpc, as shown in section 4. Instead, we will use a scaled version of the measurement from SDSS, using a cluster luminosity function and our knowledge of the depths of both surveys.

Shown in Fig. 4 is the $dN/dmag$ distribution of SDSS shape catalog galaxies in an r_{200} annulus around the GM-BCG clusters with the average $dN/dmag$ from the whole catalogue subtracted (after scaling to the appropriate area). It is obviously different from the field distribution, which can be seen by comparing with Fig. 1. For convenience, we fit a Schechter luminosity function (Schechter 1976) of the form

$$\frac{dN}{dm} = 0.4 \ln(10) \phi^* 10^{0.4(m^* - m)(\alpha + 1)} \exp[-10^{0.4(m^* - m)}] \quad (19)$$

to the apparent magnitudes using a least-squares fit, fixing α to -1.1 in agreement with previous studies of the cluster luminosity function (see, e.g. the list in Zenteno et al. 2011). This is not a true luminosity function, since it is a function of apparent magnitudes rather than absolute magnitudes or luminosities; we use it here merely as a convenience, but these results should not be used to predict the luminosity function at other redshift ranges.

There is large covariance between the fitted ϕ^* and m^* , but altering the parameters in tandem along the degeneracy direction results in similar predictions at fainter magnitudes. Since the quantity of interest is the extrapolated curve, not

² <http://dls.physics.ucdavis.edu/~scranton/SDSSPix/>

³ <http://cfhtlens.org/>

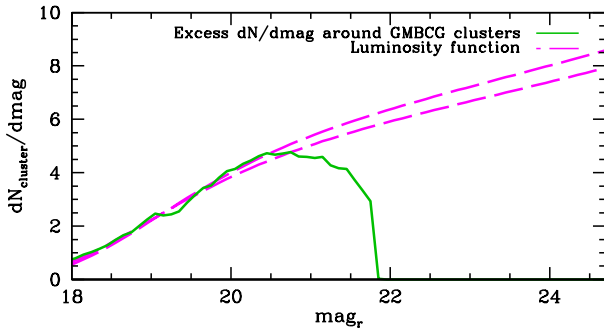


Figure 4. Redshift distribution $dN/dmag$ measurements for galaxies in SDSS located in areas near GMBCG galaxy clusters, after the field galaxy $dN/dmag$ has been subtracted. Two sample luminosity function fits are shown, which differ in amplitude but are similar to ~ 10 per cent under integration to the CFHTLenS limiting magnitude of 24.7.

the exact details of the cluster luminosity function, choosing the best-fit measurement is sufficient for our purposes. The selection of a range of points to be fit by the luminosity function matters more—the low magnitude end is dominated by the BCGs, which are not well fit by the luminosity function (Zenteno et al. 2011), and the high end turnover is dominated by our source selection and not the clusters themselves. Still, varying these endpoints within reasonable parameters gives similar results: extending the luminosity function to the CFHTLenS magnitude limit of 24.7 gives ≈ 3 times as many cluster galaxies as would be seen in SDSS. (A sample high and low fit are shown in Fig. 4.) We will therefore use the excess number density from the SDSS catalogue, times three, for our cluster galaxy distribution in CFHTLenS, though we will present some additional tests that validate this procedure as well. We assume that the cluster galaxies at fainter magnitudes have the same spatial distribution as the bright galaxies, which is in line with previous studies finding no luminosity segregation in clusters (e.g. Pracy et al. 2005).

We will also show, for comparison, some measurements around GMBCG clusters in the CFHTLenS region. These were masked using a simple geometric mask fit to the CFHTLenS area, which is made of sums of rectangles. We use the Mangle software (Swanson et al. 2008) to generate randoms in the overlap regions between the GMBCG mask (represented as simple polygons, a small approximation given the small spatial extent of the CFHTLenS mask) and the CFHTLenS mask.

4 RESULTS

First, we must measure f_{obs} , the fraction of sky obscured by the galaxies within the cluster. This is the product of the number density of galaxies within the cluster n_{cl} and the average obscured area per galaxy A_{gal} . The number density of galaxies within the cluster is simple: we measure the galaxy density around random points and around clusters; the observed number density is the number density of cluster galaxies minus the number density of non-cluster galaxies which can be detected in the same region. This is the number density around random galaxies suppressed by the

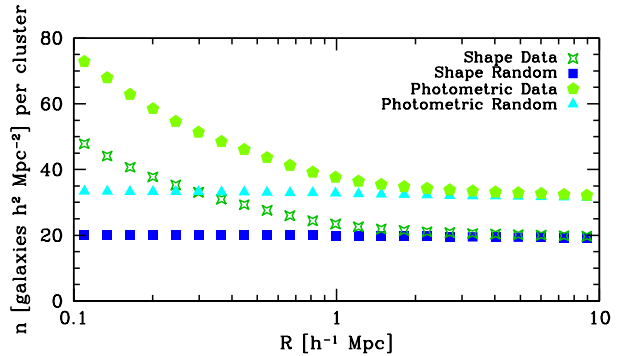


Figure 5. Number density of SDSS galaxies at all redshifts around GMBCG clusters and random points. Both the shape and photometric catalogues are shown. As expected, the number density is largest at the smallest radii. Error bars are smaller than the point size at all radii and are omitted for clarity.

obscuration of the cluster and by the magnification.

$$n_{\text{cl}} = n_{\text{obs}} - (1 + q\kappa)n_{\text{rand}}(1 - n_{\text{cl}}A_{\text{gal}}) \quad (20)$$

$$n_{\text{cl}} = \frac{n_{\text{obs}} - (1 + q\kappa)n_{\text{rand}}}{1 - (1 + q\kappa)n_{\text{rand}}A_{\text{gal}}}$$

We use n_{rand} and not n_{bg} since blending effects can remove both foreground and background galaxies, and since the magnification factor $q\kappa$ is 0 for foreground galaxies (which must be accounted for when measuring an average κ or Σ_{cr}^{-1} for all galaxies in the sample). In a real analysis, this will need to be solved iteratively or jointly for κ and the cluster mass. However, as we will show shortly, $1 + q\kappa$ is nearly 1 in SDSS for the scales on which we are making this measurement, so we will not include it in our measurement here.

We show the measurements of n_{obs} and n_{rand} and their difference in the shape and photometric catalogues for SDSS in Fig. 5 and in CFHTLenS in Fig. 6. We also show a comparison of the difference between the two curves in Fig. 7. The suppression of galaxy density due to the data reduction procedure in CFHTLenS can be seen even at moderate radii, which cannot be explained by magnification (which should increase the galaxy density given the value of q). Due to this difficulty, and to the increased stochasticity from the smaller number of clusters in the smaller CFHTLenS area, we will use a scaled version of the curve from SDSS based on the cluster luminosity function (as described in section 3.4) for the rest of our predictions involving the CFHTLenS shape catalogue. The results in this figure above $0.8h^{-1}\text{Mpc}$ suggest that this rescaling factor is indeed valid.

To convert from the number of galaxies to the obscured fraction of the sky, we must characterize the fraction of sky obscured per cluster galaxy. This obscuration comes from the observed size of the galaxy after PSF convolution, and from decisions made during the course of the deblending procedure. As a result, it varies from telescope to telescope and from data reduction method to data reduction method even when the galaxy population is identical. We consider several possible choices for the deblending-relevant area, covering a range that should capture the characteristics of most pipelines.

For CFHTLenS, the deblending issue is the dominant concern for galaxy size. CFHTLenS shapes are measured on

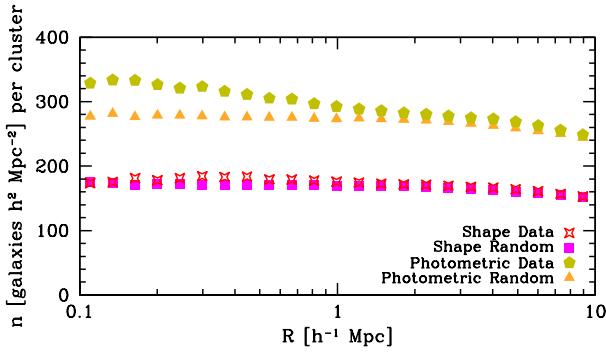


Figure 6. Number density of CFHTLenS galaxies at all redshifts around GMBCG clusters and random points. Both the shape and photometric catalogues are shown. In the photometric catalogue, the number density increases towards small radii, although the magnitude of the change is smaller than expected. In the shape catalogue, the effects of the conservative deblender can be seen as the turnover in the excess galaxy density around clusters, returning to the field level or even slightly below it for the smallest radii.

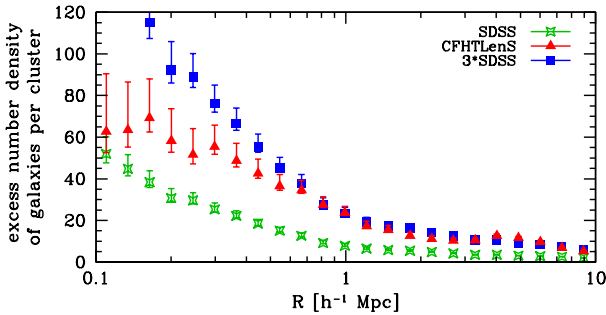


Figure 7. The excess galaxy density around GMBCG clusters, as computed by subtracting the randoms curve from the cluster curve in Figs. 5 and 6. Results from the photometric catalogues of SDSS and CFHTLenS are shown, as well as SDSS scaled to the expected number of cluster member galaxies in CFHTLenS as described in section 3.4. We have used here a measurement of SDSS only around the 427 clusters in the CFHTLenS region to remove any differences caused by the redshift and richness distribution of the small CFHTLenS subsample of the GMBCG catalogue. The prediction based on SDSS holds up well at large radii, but the suppression of galaxy counts due to the data reduction can be seen at small radii.

postage stamps of size 48×48 pixels (about $9 \times 9''$). No deblending attempts are made if a nearby galaxy is close enough that masking it out disturbs the isophotes of the target galaxy. Instead, the galaxy is excluded from the final catalogue. This procedure removes about 20 per cent of the galaxy sample. The CFHTLenS team estimates this will bias lensing signals below $5''$ (Miller et al. 2013), or approximately half the width of the postage stamp, so we can assume the deblending-relevant galaxy size is something of this order. In comoving coordinates at the redshifts of the GMBCG clusters, a length of $4.5''$ corresponds to $20h^{-1}$ kpc. As an alternate statistic, we can also measure the apparent size of the PSF-convolved galaxies in this sample. This is a redshift-dependent quantity, since the size of the PSF will increase with angular diameter distance in either phys-

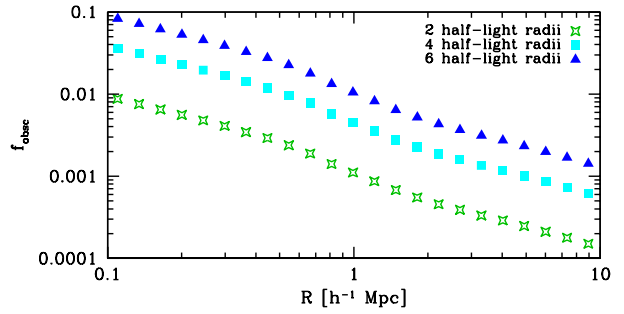


Figure 8. Fraction of the sky obscured by cluster galaxies as a function of radius in SDSS for several choices of sky area per galaxy. The curves are almost self-similar, but there are small effects due to the correction of Eq. 20.

ical or comoving coordinates. The full width at half max (FWHM) of the CFHTLenS galaxies, assuming a Gaussian core, is given in the shape catalogue, so we can measure the average comoving area of the galaxy+PSF within the FWHM circle. We find the average area to be $36h^{-2}\text{kpc}^2$ for all CFHTLenS galaxies from 0.1-0.55 weighted (by BPZ maximum likelihood redshift) to match the redshift distribution of the GMBCG clusters, which corresponds to a radius of $3.4h^{-1}$ kpc. This is quite a bit larger than the average galaxy radius in the same redshift range, due to a combination of averaging r^2 rather than r and the contribution of the PSF size.

For SDSS, where the direct measurement of the combined galaxy+PSF FWHM was not saved post-processing, we use the resolution factor, Eq. 16. The traces of the moments matrices T_I and T_P are second-moment measurements, and should be roughly proportional to the area. We can then use the measurement of the PSF FWHM at each galaxy position to write

$$A_{\text{FWHM}} = \frac{\pi(\text{FWHM}/2)^2}{1 - R_2}, \quad (21)$$

where we use only the r -band measurements for simplicity. We find this area is $78 \times h^{-2}\text{kpc}^2$, again matched to the GMBCG redshift range, corresponding to a PSF-convolved half-light radius of $5.0h^{-1}$ kpc.

Since the exact details of the deblender will affect how many half-light radii we can consider the galaxy to obscure, we will show results for galaxy areas corresponding to 2, 4 and 6 times the half-light radius for SDSS and CFHTLenS, as well as an area corresponding to a radius of $1/2$ the postage stamp size for CFHTLenS only given the choices made in its deblending process. Combining the size of an average cluster galaxy and the number density of cluster galaxies, we can compute $f_{\text{obs}}(R)$, as shown in Fig. 8. Assuming that measurements of stacked lensing are made using number densities around random points to correct for dilution by physically-associated sources, and that magnification estimates likewise neglect the obscuration effect, we find systematic errors in the shear as shown in Figs. 9 (SDSS) and 10 (CFHTLenS) and magnification errors as shown in Fig. 11 (both surveys).

The fraction of the sky obscured by the cluster galaxies depends strongly on the assumed area obscured per galaxy. Even at our most conservative estimate, however, this is a 1

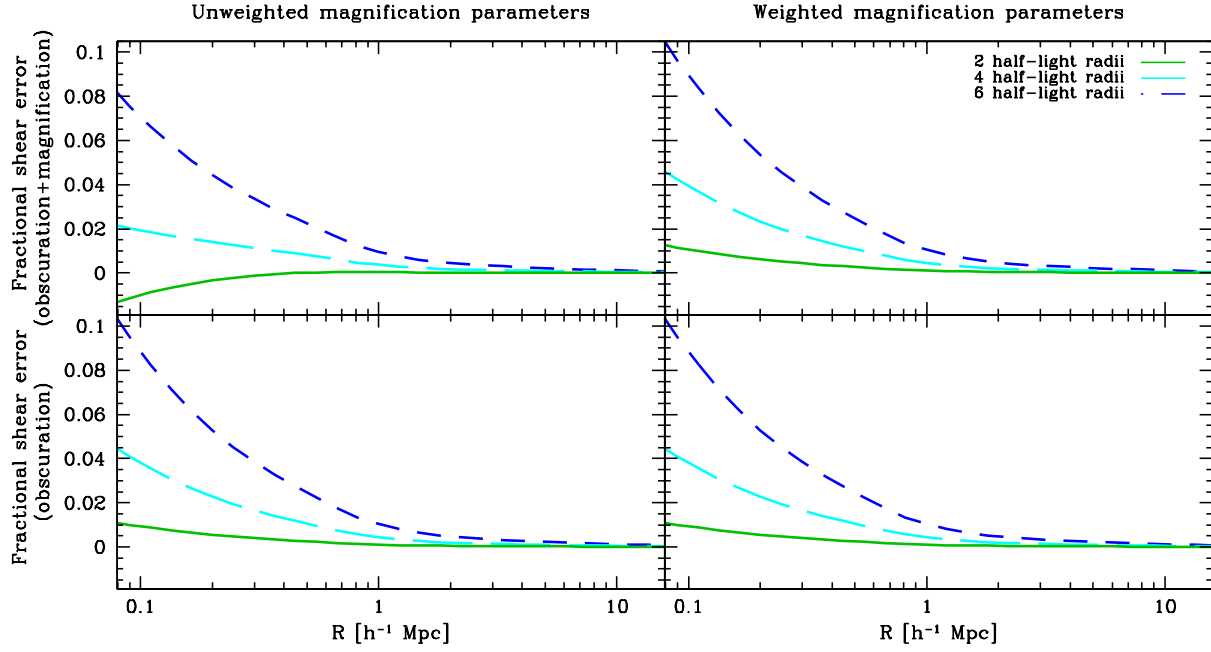


Figure 9. Fractional errors on the shear in an SDSS-like survey due to neglecting magnification and obscuration (top) or neglecting obscuration only (bottom). Magnification parameters derived using unweighted galaxy densities are shown in the left-hand column, and using weighted densities in the right-hand column. Galaxies magnified just above detection limits are so heavily downweighted in this sample that the magnification has only a negligible effect when weights are included. The obscuration can be quite large, up to order 10 per cent in the centers of the clusters for conservative deblenders.

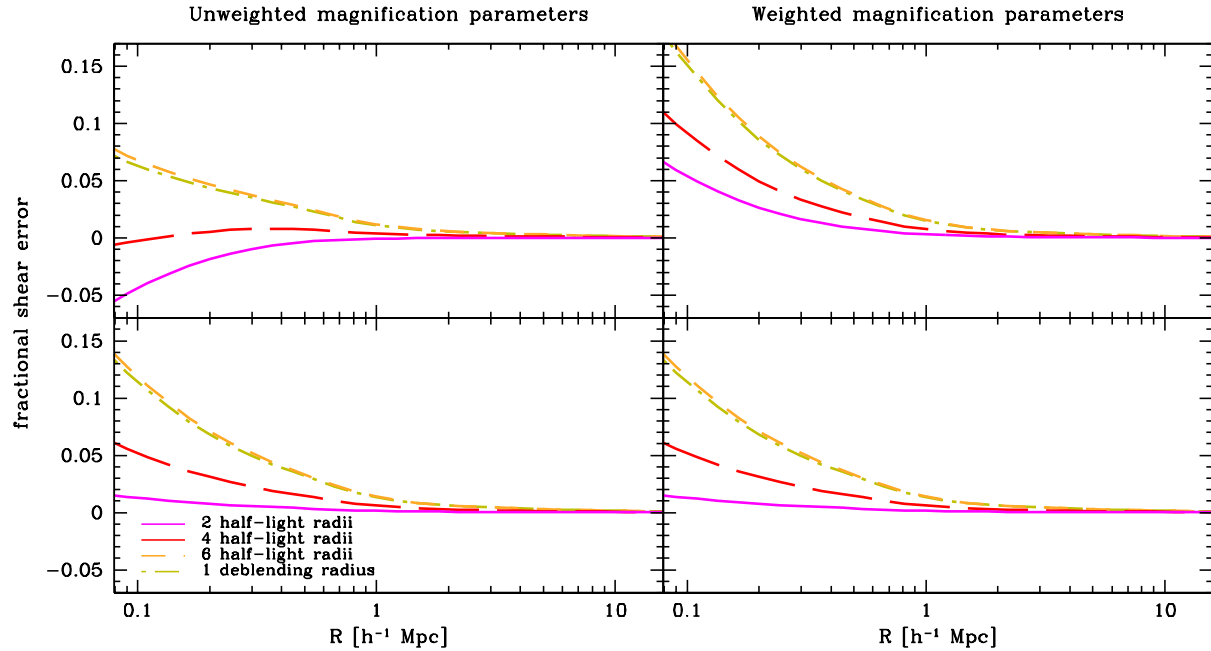


Figure 10. Fractional errors on the shear in a CFHTLenS-like survey due to neglecting magnification and obscuration (top) or neglecting obscuration only (bottom). All curves are derived using a scaled version of the SDSS obscuration, Fig. 8, due to the difficulty of measuring the obscuration in CFHTLenS. Magnification parameters derived using unweighted galaxy densities are shown in the left-hand column, and using weighted densities in the right-hand column. The magnification is more important in this survey than in SDSS, unsurprising given the depth. Like SDSS, the obscuration is important in the centers of the clusters.

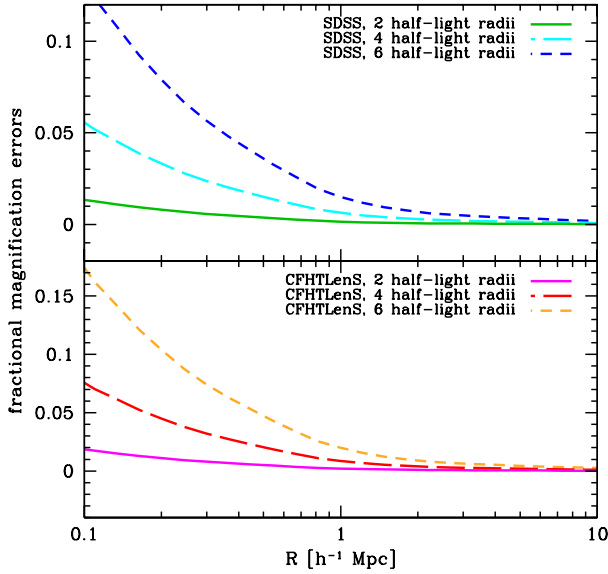


Figure 11. Fractional errors on the magnification in SDSS-like (top) and CFHTLenS-like (bottom) photometric surveys for a range of obscuration areas per galaxy, assuming that the magnification can be measured in narrow annular bins. Since *lensfit* was not used for the photometric catalog, no deblending radius is shown for the CFHTLenS sample.

per cent effect for the inner regions of GMBCG-like clusters in current surveys. We would naively expect this problem to increase with depth, as more galaxies can be detected; however, since most of the galaxies have a size dominated by the PSF, a survey with better seeing can counteract this increase by reducing the observed sizes for all galaxies, even the ones detected in the shallower survey. By coincidence, these two effects (more galaxies but smaller PSF) nearly cancel when moving from SDSS to CFHTLenS for a given choice of deblend radius, and we see similar obscuration predictions for both surveys in the bottom right panels of Figures 9 and 10. However, since the two surveys do not make the same choices about deblending, the effect will not actually be the same for their measurements in practice.

Also of interest is the effect of magnification on the shear errors, which can be seen by comparing the top and bottom rows in Figures 9 and 10. In a CFHTLenS-like survey that measures lensing around massive clusters, the magnification can change densities by a few per cent in the inner regions of the cluster, which will impact the boost factor and thus the shear by a similar amount. Unlike the obscuration, however, this depends on the mass and mass distribution assumed or measured for the clusters, so it is not as easy to separate from the measurement of interest. The difference between the expected magnification if the parameters are measured using the same shape weights as the galaxy or not are large as well, highlighting the importance of correctly weighting the number densities when computing the magnification.

Finally, the obscuration effect can also be seen in a pure magnification measurement. The effect is larger because more galaxies (including cluster galaxies) are detected in the photometric catalogues, where magnification measurements will be made. We assume here that the measure-

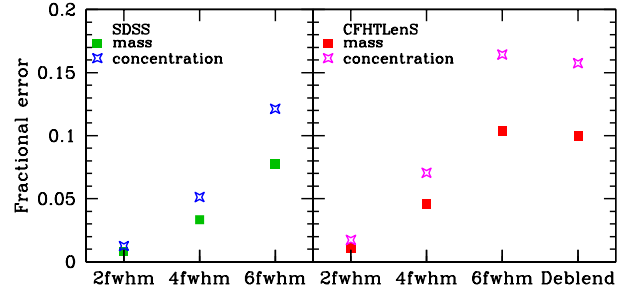


Figure 12. Fractional errors on the derived mass and concentration for a $10^{14} h^{-1}$ solar mass halo with concentration 4, using a two-component NFW fit to false shear data made using a perfect input NFW halo modified by the obscuration measurements of Figs. 9 and 10. Fits were made in the radius range $0.1 - 2h^{-1}$ Mpc to avoid the two-halo regime. One-sigma error bars in logarithmically-spaced annuli were assumed to be proportional to $1/r$, as is the case for shape noise-dominated errors. Different choices of radii to use or error distributions for weighting the fits will change the impact of this effect.

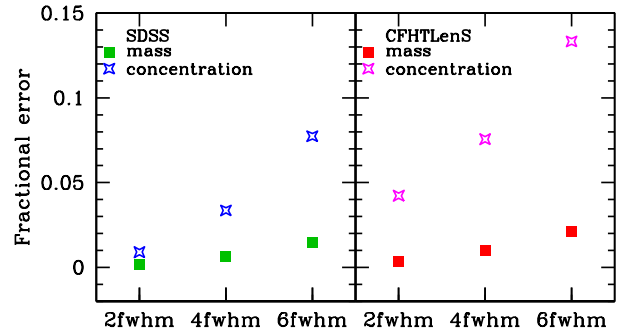


Figure 13. Fractional errors on the derived mass and concentration for a $10^{14} h^{-1}$ solar mass halo with concentration 4, using a two-component NFW fit to false magnification data made using a perfect input NFW halo modified by the obscuration measurements of Fig. 11. Fits were made in the radius range $0.1 - 2h^{-1}$ Mpc to avoid the two-halo regime, and assume that the measurement can be made in narrow annular bins like the shear can. One-sigma error bars were assumed to be proportional to $1/r$. Different annulus bins or error distributions will change the impact of this effect.

ment can be made in annular bins with the same resolution as the shear measurements.

These effects will propagate into measurements of cluster masses and concentrations. We show the mass and concentration errors caused by the (uncorrected) obscuration effect in Fig. 12 (shear) and Fig. 13 (magnification). These are fractional errors on both quantities assuming a joint NFW fit to a perfect NFW input. The effect is within the error budgets for current measurements with SDSS, but is troublesome for CFHTLenS, where there are published cluster masses measured to approximately 10 per cent with magnification (Ford et al. 2014). The mass errors are lessened by approximately 20 per cent if we fix the concentration to the input value, since we reduce our sensitivity to the radial dependence of the obscuration, but as the concentration may also be a parameter of interest in cluster studies we show only the errors from the joint fit.

Survey	Depth	$N_{\text{gals}}/N_{\text{gals,SDSS}}$	PSF FWHM (")	Projected galaxy FWHM radius (kpc)
HSC	25.1	3.5	0.6	2.4
DES	24.3	3	0.9	3.8
Euclid	24.5	3	≤ 0.18	0.73
LSST	27.5	5.5	0.7	2.8

Table 2. Relevant survey parameters for the four surveys we use for projecting the obscuration effect: HSC, DES, Euclid, and LSST. Depth is reported in the band intended for weak lensing imaging: i for HSC and DES, broad-band visual for Euclid, r or i for LSST. Where available the depth is the depth used in discussions of galaxy detections, generally the 10σ extended-source detection limit. The HSC predictions only report 5σ detections at a magnitude of 25.9, so we assume a factor of 2 brighter for a 10σ detection (a more fair comparison to the other surveys) yielding a magnitude of 25.1. The listed Euclid PSF FWHM is the upper limit of the weak lensing requirement for the survey as in Laureijs et al. (2011), and allows for sources of PSF broadening such as jitter and charge diffusion that makes the PSF wider than the nominal expectation given the diffraction limit of the telescope and bandpass. $N_{\text{gals}}/N_{\text{gals,SDSS}}$ is a prediction based on our fit to the cluster luminosity function, Eq. 19, rounded to the nearest half integer. Galaxy radius is a prediction based on the survey PSF, since the PSF-convolved size is the relevant quantity here.

5 FORECASTS FOR THE IMPACT OF OBSCURATION ON FUTURE SURVEYS

We can make rough predictions for how future surveys will be impacted by this effect for GMBCG-like cluster catalogues. As with our CFHTLenS calculation above, we need only know the average size of a PSF-convolved galaxy and the depth of the imaging. Then we can project the cluster luminosity function to various depths in order to predict the galaxy number density and multiply by the area to predict the obscuration fraction. In the case of shear estimates, these predictions are relevant in the case that the photo- z are sufficiently imperfect that it is necessary to remove the dilution due to source galaxies that are physically associated with the lenses (rather than normalizing by the actual number of background galaxies used). The estimates of the impact on magnification measurements are more general.

We make predictions for four surveys: the Hyper Suprime-Cam survey (HSC, Miyazaki et al. 2012); the Dark Energy Survey (DES, The Dark Energy Survey Collaboration 2005), which recently measured this effect for four clusters in Melchior et al. (2014); Euclid (Laureijs et al. 2011); and the Large Synoptic Survey Telescope (LSST, LSST Science Collaboration et al. 2009). DES, HSC and LSST are ground-based surveys, while Euclid is a space-based survey; DES and HSC are already taking data as of the publication date of this paper, while Euclid and LSST will begin in the early 2020s. All four of these surveys will engage in large-scale surveys of the sky with cosmology as a principal aim, and have both weak lensing and galaxy cluster science among the main science drivers of the survey goals. We summarize the relevant depth and PSF information in Table 2.

The average galaxy size will generally be dominated by the PSF, given the power-law distribution of galaxy sizes.

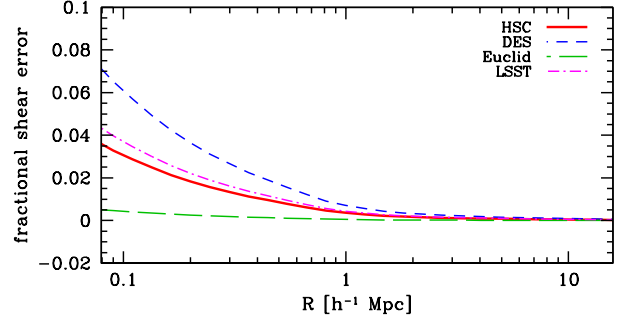


Figure 14. Estimates of the fractional systematic errors on the shear in several upcoming surveys due to neglect of the obscuration effect around GMBCG-like clusters. The number of galaxies in the cluster is the number in the SDSS catalogue scaled according to the cluster luminosity function, Eq. 19; the deblending-relevant average galaxy radius is assumed to be 8 times the survey PSF FWHM, which is a typical number based on the results from SDSS and CFHTLenS. The surveys are close enough in depth that the PSF size dominates, giving DES the largest errors due to this effect and Euclid, a space-based survey, the smallest.

However, since we are interested in area rather than radius (which favors larger galaxies) and since surveys with smaller PSFs can resolve galaxies below the PSF size for the surveys with worse seeing, the average galaxy size is not simply proportional to the FWHM or the FWHM squared. We find that SDSS galaxies have a mean FWHM area approximately 3.5 times the FWHM area of the PSF, and CFHTLenS galaxies have a mean FWHM area approximately 6 times the FWHM area of the PSF. For simplicity, we assume upcoming surveys will have galaxy areas ≈ 4 times the area of their PSFs.

We can rescale the obscuration signal around GMBCG clusters in SDSS by these numbers. Fig. 14 shows the systematic errors on the shear for future surveys that measure cluster lensing without accounting for obscuration, assuming a galaxy deblend area with a radius 4 times the galaxy FWHM radius (8 times the PSF FWHM) and a GMBCG-like mass and redshift distribution. The effect is worst in DES, given the combination of a deep survey with a larger PSF. It is hardly detectable in Euclid given the small space-based PSF. The shape of the PSF and not its FWHM may be more important for diffraction-limited space-based surveys, which could alter the predicted size of the effect, but our prediction for the size of this effect is so small that even factors of ~ 2 changes would not alter the essential conclusion that this effect is not a substantial source of systematic error for Euclid lensing analysis of clusters in the $\sim 10^{14} h^{-1} M_{\odot}$ mass range.

All the ground-based surveys have a maximum shear error of $\gtrsim 5$ per cent at the minimum radius we consider ($0.1 h^{-1} \text{Mpc}$). We can see from Fig. 12 that the error on the mass is of comparable size to the maximum shear error, so neglecting the obscuration effect may impact cluster mass estimates to nearly that level—an important effect for all of these surveys given that they are trying to push stacked cluster mass measurements below 10 per cent errors.

We can compare this prediction to the effect that has recently been observed in the Dark Energy Survey by Melchior et al. (2014). The galaxy clusters studied in that

work are slightly lower-redshift than the GMBCG clusters (redshifts $\approx 0.3\text{--}0.4$ for three of the clusters, versus the peak GMBCG redshift of 0.45 ; the fourth cluster is the nearby Abell 3216). They are also more massive⁴, with the three distant clusters all $\geq 10^{15}h^{-1}$ solar masses. The nearness of the clusters will slightly counteract the obscuration effect (since galaxies convolved with the same angular size PSF will look smaller in physical units at smaller z). The mass will increase it, though, by adding more cluster galaxies. The mass is usually found to be proportional to the number of galaxies above a luminosity threshold as approximately $N_{\text{gals}}^{1.1-1.2}$, so we can expect in turn that the number of galaxies will be proportional to $M_{\text{cl}}^{0.8-0.9}$, giving us a factor of $\sim 6\text{--}8$ in number of galaxies and thus obscuration, or 50 to 70 per cent obscuration at $0.1h^{-1}$ Mpc ignoring redshift effects, while Melchior et al. report a criterion equivalent to approximately 40 to 60 per cent obscuration as well, a reasonable level of agreement given the degree of estimation involved.

The effect is also measured differently in Melchior et al.. They measure the obscured fraction of the sky directly, by using the BALROG software⁵ to add a simulated galaxy to the measured data and then checking if the pipeline detects the new galaxy or not. This also captures other effects such as problems in background subtraction in dense regions, and is probably the most formally correct way to solve the problem. However, once the average deblending size of galaxies as a function of redshift is measured, our method of predicting the impact of obscuration on cluster shear and magnification measurements essentially comes for free with any $\Delta\Sigma$ computation, and may be more computationally feasible for large, heterogeneous cluster samples.

6 CONCLUSIONS

We have presented an analysis of the impact on weak lensing shear and magnification measurements of galaxy clusters due to the obscuration of the background sky caused by galaxies within those same clusters due to the difficulty of separating nearby galaxies. The effect is small enough to be within the error budgets of current surveys, with the possible exception of CFHTLenS given its conservative deblending choices, but it is large enough to become important as deeper surveys try to reach better precision on their galaxy cluster mass estimates. Thus, schemes for accounting for this effect, such as that used by Melchior et al. (2014), should be incorporated into the cluster lensing measurements of future surveys. Since the effect is a function of radius, it impacts both the mass and concentration estimates for the clusters in nonlinear ways.

The precise size of the effect is difficult to compute.

⁴ While no mass measurements have been made for GMBCG, the similar MaxBCG catalog (Koester et al. 2007) contains clusters with a typical mass of $\approx 10^{14}h^{-1}$ solar masses (Mandelbaum et al. 2008). Both catalogs have a similar comoving number density of approximately $2 \times 10^{-5}h^3\text{Mpc}^{-3}$, and transforming the richness estimator of GMBCG into the MaxBCG richness estimator and applying the scaling relation of Mandelbaum et al. (2008) also yields cluster masses of this order.

⁵ <https://github.com/emhuff/Balrog>

For our method, the number of cluster galaxies must be measured, which is not difficult as long as the obscuration leaves a majority of the objects measured. However, the average area covered by a galaxy is subtle, as it relies on the details of the galaxy light distribution, the effect of the PSF convolution, and the success of the deblending software at disentangling nearby objects. Detailed analysis of deblender behavior on realistic galaxies will be required to compute the size of this effect in real data. However, a rough estimate of the effect size, based on simple arguments, shows that obscuration will be important for deeper surveys with more precise mass measurement targets. Corrections for obscuration will be necessary for upcoming surveys to meet their requirements on cluster mass estimates using stacked lensing and clustering measurements.

7 ACKNOWLEDGEMENTS

This work was supported by the Department of Energy Early Career Award program.

We thank Ying Zu, Mike Jarvis, Eduardo Rozo, Fabian Schmidt, Ross O’Connell, and Mariana Vargas-Margaña for useful discussions related to this work.

Funding for the SDSS and SDSS-II has been provided by the Alfred P. Sloan Foundation, the Participating Institutions, the National Science Foundation, the U.S. Department of Energy, the National Aeronautics and Space Administration, the Japanese Monbukagakusho, the Max Planck Society, and the Higher Education Funding Council for England. The SDSS Web Site is <http://www.sdss.org/>. The SDSS is managed by the Astrophysical Research Consortium for the Participating Institutions. The Participating Institutions are the American Museum of Natural History, Astrophysical Institute Potsdam, University of Basel, University of Cambridge, Case Western Reserve University, University of Chicago, Drexel University, Fermilab, the Institute for Advanced Study, the Japan Participation Group, Johns Hopkins University, the Joint Institute for Nuclear Astrophysics, the Kavli Institute for Particle Astrophysics and Cosmology, the Korean Scientist Group, the Chinese Academy of Sciences (LAMOST), Los Alamos National Laboratory, the Max-Planck-Institute for Astronomy (MPIA), the Max-Planck-Institute for Astrophysics (MPA), New Mexico State University, Ohio State University, University of Pittsburgh, University of Portsmouth, Princeton University, the United States Naval Observatory, and the University of Washington.

This work is based on observations obtained with MegaPrime/MegaCam, a joint project of CFHT and CEA/IRFU, at the Canada-France-Hawaii Telescope (CFHT) which is operated by the National Research Council (NRC) of Canada, the Institut National des Sciences de l’Univers of the Centre National de la Recherche Scientifique (CNRS) of France, and the University of Hawaii. This research used the facilities of the Canadian Astronomy Data Centre operated by the National Research Council of Canada with the support of the Canadian Space Agency. CFHTLenS data processing was made possible thanks to significant computing support from the NSERC Research Tools and Instruments grant program.

REFERENCES

- Aihara H., et al., 2011, *ApJs*, 193, 29
- Albrecht A., Bernstein G., Cahn R., Freedman W. L., Hewitt J., Hu W., Huth J., Kamionkowski M., Kolb E. W., Knox L., Mather J. C., Staggs S., Suntzeff N. B., 2006, *ArXiv Astrophysics e-prints*
- Allen S. W., Evrard A. E., Mantz A. B., 2011, *ARA&A*, 49, 409
- Applegate D. E., von der Linden A., Kelly P. L., Allen M. T., Allen S. W., Burchat P. R., Burke D. L., Ebeling H., Mantz A., Morris R. G., 2014, *MNRAS*, 439, 48
- Bartelmann M., Schneider P., 2001, *Phys. Rep.*, 340, 291
- Benítez N., 2000, *ApJ*, 536, 571
- Bernstein G., Huterer D., 2010, *MNRAS*, 401, 1399
- Bernstein G. M., Jarvis M., 2002, *AJ*, 123, 583
- Bertin E., Arnouts S., 1996, *A&AS*, 117, 393
- Blazek J., Mandelbaum R., Seljak U., Nakajima R., 2012, *JCAP*, 5, 41
- Bridle S., et al., 2010, *MNRAS*, 405, 2044
- Capak P. L., 2004, PhD thesis, UNIVERSITY OF HAWAII
- Coe D., Benítez N., Sánchez S. F., Jee M., Bouwens R., Ford H., 2006, *AJ*, 132, 926
- Corless V. L., King L. J., 2007, *MNRAS*, 380, 149
- Erben T., et al., 2013, *MNRAS*, 433, 2545
- Feldmann R., et al., 2006, *MNRAS*, 372, 565
- Ford J., Hildebrandt H., Van Waerbeke L., Erben T., Laigle C., Milkeraitis M., Morrison C. B., 2014, *MNRAS*, 439, 3755
- George M. R., Leauthaud A., Bundy K., Finoguenov A., Ma C.-P., Rykoff E. S., Tinker J. L., Wechsler R. H., Massey R., Mei S., 2012, *ApJ*, 757, 2
- Hamana T., Oguri M., Shirasaki M., Sato M., 2012, *MNRAS*, 425, 2287
- Hao J., McKay T. A., Koester B. P., Rykoff E. S., Rozo E., Annis J., Wechsler R. H., Evrard A., Siegel S. R., Becker M., Busha M., Gerdes D., Johnston D. E., Sheldon E., 2010, *ApJs*, 191, 254
- Heymans C., et al., 2012, *MNRAS*, 427, 146
- Heymans C., et al., 2013, *MNRAS*, 432, 2433
- Hildebrandt H., et al., 2012, *MNRAS*, 421, 2355
- Hirata C., Seljak U., 2003, *MNRAS*, 343, 459
- Hirata C. M., Seljak U., 2004, *PRD*, 70, 063526
- Hoekstra H., Hartlap J., Hilbert S., van Uitert E., 2011, *MNRAS*, 412, 2095
- Kitching T. D., et al., 2012, *MNRAS*, 423, 3163
- Koester B. P., et al., 2007, *ApJ*, 660, 239
- Kravtsov A. V., Borgani S., 2012, *ARA&A*, 50, 353
- Laureijs R., Amiaux J., Arduini S., Auguères J., Brinchmann J., Cole R., Cropper M., Dabin C., Duvet L., Ealet A., et al. 2011, *ArXiv e-prints*
- LSST Science Collaboration Abell P. A., Allison J., Anderson S. F., Andrew J. R., Angel J. R. P., Armus L., Arnett D., Asztalos S. J., Axelrod T. S., et al. 2009, *ArXiv e-prints*
- Lupton R., Gunn J. E., Ivezić Z., Knapp G. R., Kent S., 2001, in Harnden Jr. F. R., Primini F. A., Payne H. E., eds, *Astronomical Data Analysis Software and Systems X* Vol. 238 of Astronomical Society of the Pacific Conference Series, The SDSS Imaging Pipelines. p. 269
- Mandelbaum R., Hirata C. M., Seljak U., Guzik J., Padmanabhan N., Blake C., Blanton M. R., Lupton R., Brinkmann J., 2005, *MNRAS*, 361, 1287
- Mandelbaum R., Seljak U., Baldauf T., Smith R. E., 2010, *MNRAS*, 405, 2078
- Mandelbaum R., Seljak U., Cool R. J., Blanton M., Hirata C. M., Brinkmann J., 2006, *MNRAS*, 372, 758
- Mandelbaum R., Seljak U., Hirata C. M., 2008, *JCAP*, 8, 6
- Marian L., Smith R. E., Bernstein G. M., 2010, *ApJ*, 709, 286
- Massey R., Hoekstra H., Kitching T., Rhodes J., Cropper M., Amiaux J., Harvey D., Mellier Y., Meneghetti M., Miller L., Paulin-Henriksson S., Pires S., Scaramella R., Schrabback T., 2013, *MNRAS*, 429, 661
- Melchior P., et al., 2014, *ArXiv e-prints*
- Miller L., et al., 2013, *MNRAS*, 429, 2858
- Miyazaki S., et al., 2012, in Society of Photo-Optical Instrumentation Engineers (SPIE) Conference Series Vol. 8446 of Society of Photo-Optical Instrumentation Engineers (SPIE) Conference Series, Hyper Suprime-Cam
- Nakajima R., Mandelbaum R., Seljak U., Cohn J. D., Reyes R., Cool R., 2012, *MNRAS*, 420, 3240
- Parker L. C., Hoekstra H., Hudson M. J., van Waerbeke L., Mellier Y., 2007, *ApJ*, 669, 21
- Pracy M. B., Driver S. P., De Propriis R., Couch W. J., Nulsen P. E. J., 2005, *MNRAS*, 364, 1147
- Reyes R., Mandelbaum R., Gunn J. E., Nakajima R., Seljak U., Hirata C. M., 2012, *MNRAS*, 425, 2610
- Rozo E., Wu H.-Y., Schmidt F., 2011, *ApJ*, 735, 118
- Schechter P., 1976, *ApJ*, 203, 297
- Schmidt F., Rozo E., Dodelson S., Hui L., Sheldon E., 2009, *Physical Review Letters*, 103, 051301
- Schneider M. D., Frenk C. S., Cole S., 2012, *JCAP*, 5, 30
- Sheldon E. S., Cunha C. E., Mandelbaum R., Brinkmann J., Weaver B. A., 2012, *ApJS*, 201, 32
- Sheldon E. S., Johnston D. E., Frieman J. A., Scranton R., McKay T. A., Connolly A. J., Budavári T., Zehavi I., Bahcall N. A., Brinkmann J., Fukugita M., 2004, *AJ*, 127, 2544
- Sheldon E. S., Johnston D. E., Scranton R., Koester B. P., McKay T. A., Oyaizu H., Cunha C., Lima M., Lin H., Frieman J. A., Wechsler R. H., Annis J., Mandelbaum R., Bahcall N. A., Fukugita M., 2009, *ApJ*, 703, 2217
- Stoughton C., et al., 2002, *AJ*, 123, 485
- Swanson M. E. C., Tegmark M., Hamilton A. J. S., Hill J. C., 2008, *MNRAS*, 387, 1391
- The Dark Energy Survey Collaboration 2005, *ArXiv Astrophysics e-prints*
- Voit G. M., 2005, *Reviews of Modern Physics*, 77, 207
- Weinberg D. H., Mortonson M. J., Eisenstein D. J., Hirata C., Riess A. G., Rozo E., 2013, *Phys. Rep.*, 530, 87
- Wright C. O., Brainerd T. G., 2000, *ApJ*, 534, 34
- York D. G., et al., 2000, *AJ*, 120, 1579
- Zenteno A., et al., 2011, *ApJ*, 734, 3